

REVIEWS OF TOPICAL PROBLEMS

PACS numbers: 33.20.Fb, **42.70. – a,** 42.70.Mp, **61.72. – y**

Manifestation of defects and imperfections of lithium niobate crystals in Raman spectra

N.V. Sidorov, N.A. Teplyakova, M.N. Palatnikov

DOI: https://doi.org/10.3367/UFNe.2024.11.039806

Contents

Abstract. We discuss the main reasons for the appearance of low-intensity 'extra' lines (not corresponding to fundamental lattice vibrations) in the Raman spectrum of nonstoichiometric nonlinear optical $LiNbO_3$ crystals. These lines arise due to the formation of two-particle states of acoustic crystal vibrations with a zero total wave vector, strong anharmonicity of fundamental vibrations, the presence of microstructures (clusters) whose structure differs from that of the crystal matrix, the presence of microinclusions of impurity phases of other lithium niobates, and the photorefraction effect. It is shown that 'extra' Raman spectral lines can serve as a new highly sensitive tool for studying the structural perfection of $LiNbO_3$ crystals.

Keywords: lithium niobate, single crystals, Raman spectroscopy, defects, 'extra' lines, laser conoscopy, photoinduced light scattering

1. Introduction

The ferroelectric nonlinear optical single crystal of lithium niobate ($LiNbO_3$) exhibits a successful combination of unique physical characteristics: high values of the Curie point (1424 K) and spontaneous polarization (5×10^{-5} C cm^{-1}), high values of nonlinear optical coefficients ($d_{33} = 37.8 \times 10^{-12}$ m B^{-1}, $d_{31} = 5.18 \times 10^{-12}$ m B^{-1}, $d_{22} = 2.468 \times 10^{-12}$ m B^{-1}), high radiation resistance, as well as the photorefraction effect (optical damage), which can be controlled over a wide range by doping and changing the stoichiometry [1–12]. The band gap in an $LiNbO_3$ crystal is close to that in wide-bandgap semiconductors and ranges from 3.48 to 3.73 eV, depending on the crystal composition [6]. Of all the known materials, the $LiNbO_3$ crystal has the highest electromechanical coupling coefficient [1]. The $LiNbO_3$ crystal is used to develop compact crystal accelerators [4], in information processing systems [2, 3, 7–10, 13], to generate terahertz radiation [14], in biomedicine [15], and in holography [3, 7, 8, 13]. The $LiNbO_3$ single crystal is transparent in the range of 0.25–5.3 μm, which allows it to be used in the visible, near, and mid-IR ranges. Currently, single $LiNbO_3$ crystals of congruent composition ($R = [Li]/[Nb] = 0.946$) and single $LiNbO_3$:Mg (5.5 mol% MgO) crystals are used as materials for the conversion and modulation of laser radiation. They have a significantly lower coercive field than congruent crystals do (≈ 2.3 and ≈ 23.0 kV cm^{-1}, respectively), which is important for the development of laser radiation converters on periodically polarized submicron-sized domains [16–19].

Market requirements for physical characteristics and structural perfection of functional optical elements based on $LiNbO_3$ single crystals are becoming more stringent, which calls for comprehensive studies of the state of the defective structure of crystals of different compositions and production technologies in order to optimize their physical characteristics. $LiNbO_3$ is a heterodesmic crystal and is characterized by various types of interactions between its structural units: hydrogen bond, electrostatic interaction, covalent bond. In this case, the relatively low energy hydrogen bond has a significant effect on the formation of structural features of highly perfect single crystals of stoichiometric composition, which are suitable for the manufacture of functional elements for the conversion of laser radiation by periodically polarized domains of submicron size [5, 6].

Lithium niobate is an oxygen-octahedral nonstoichiometric phase of variable composition with a high congruent melting point (1526 K) and a wide homogeneity region in the phase diagram (44.5–50.5 mol% Li_2O at 1460 K), which narrows sharply with decreasing temperature (49.5–50.5 mol% Li_2O at 293 K) (Fig. 1) [6, 7, 20–23]. Optimization

N.V. Sidorov [a], **N.A. Teplyakova** [b], **M.N. Palatnikov** [c]
Tananaev Institute of Chemistry — Subdivision of the Federal Research Centre, Kola Science Centre, Russian Academy of Sciences, Akademgorodok 26a, 184209 Apatity, Murmansk region, Russian Federation
E-mail: [a] n.sidorov@ksc.ru, [b] n.tepliakova@ksc.ru, [c] m.palatnikov@ksc.ru

Received 19 March 2024, revised 20 June 2024
Uspekhi Fizicheskikh Nauk **195** (3) 260 – 275 (2025)
Translated by E.N. Ragozin

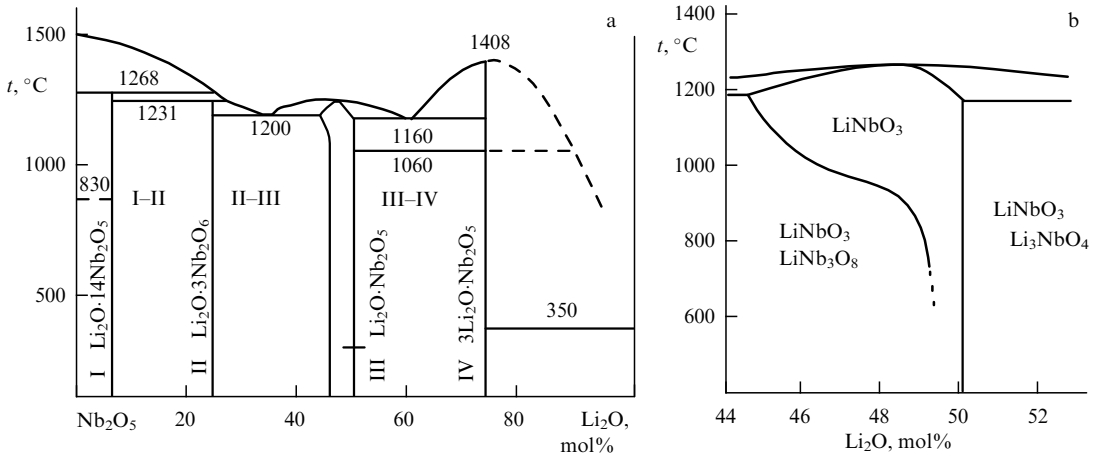

Figure 1. (a) Phase diagram of Li_2O–Nb_2O_5 system and (b) detail of the phase diagram [22].

of physical characteristics by changing the composition, structural features, and state of defects of the $LiNbO_3$ crystal is a topical fundamental problem of great applied significance. In particular, to make highly advanced optical materials for the conversion of laser radiation, research aimed at elucidating the patterns of formation of features of the defect structure of $LiNbO_3$ crystals in relation to the composition is relevant in order to obtain single crystals of high compositional homogeneity with the weakest possible photorefraction effect. The magnitude of the photorefraction effect in the $LiNbO_3$ crystal is significantly affected by point defects in the form of cations and vacancies of the cation sublattice, which are located in the crystal structure in positions other than their own, producing deep and shallow energy levels (electron traps) in the forbidden zone [6–8, 24]. The compositional homogeneity of the $LiNbO_3$ crystal is most significantly affected by extended defects in the form of microstructures (clusters) with a structure different from that of the crystalline matrix. This defect type in that of the $LiNbO_3$ crystal is currently the least studied, and experimental data from different authors are contradictory [24–38].

Point defects in the form of Nb cations located in the positions of Li cations (Nb_{Li} defect) are deep electron traps that produce localized energy levels in the forbidden zone, which enhance photorefraction [6–8]. Therefore, it is possible to reduce photorefraction in an $LiNbO_3$ crystal by decreasing the density of Nb_{Li} point defects. Usually, a reduction in the photorefraction of an $LiNbO_3$ single crystal is achieved by doping with 'nonphotorefractive' metal cations Mg, Zn, Gd, etc., which do not change their charge state when exposed to laser radiation but displace Nb_{Li} point defects from the crystal [6–8, 16]. Moreover, with double doping with different 'nonphotorefractive' metals, a reduction in photorefraction is achieved at significantly lower densities of the doping metals, and the grown single crystals are more compositionally homogeneous than with single doping [6–9, 39–44]. Furthermore, compared to single doping, double doping makes it possible to more finely control the deformation of oxygen-octahedral clusters MeO_6 ($Me = Nb$, Li: doping metal, vacancy), the ordering of structural units, and the state of defectiveness of the cation sublattice of the $LiNbO_3$ crystal along the polar axis, which determines the magnitude of spontaneous polarization and nonlinear optical properties of the crystal [7, 27]. It is also noteworthy that, with double doping, when one of the dopants is photorefractive, at a low density of this photorefractive additive (which, based on general considerations, should enhance the photorefraction effect), it is possible, on the contrary, to obtain a noticeable reduction in the photorefraction effect with a simultaneous increase in the compositional homogeneity of the crystal [27]. Also detected in highly perfect double-doped $LiNbO_3$ crystals was a noticeable increase in nonlinear optical coefficients compared to single-doped crystals [41–43]. However, doping (both single and double) leads to the occurrence of threshold effects in the $LiNbO_3$ crystal, near which the compositional homogeneity of the crystal can significantly deteriorate [27].

One of the highest sensitivity and most informative methods for studying the subtle features of the state of crystal defects is Raman spectroscopy. Raman spectra are sensitive to the slightest changes in the interactions between the structural units of the crystal. Consequently, they are sensitive to various changes in the arrangement of the structural units of the crystal, to a change in the conformation of the structural units, to a change in the state of crystal defects that occur when the crystal composition changes, to production technology, and to exposure of the photorefractive crystal to laser radiation (photoinduced defects). When polarized laser radiation passes through a photorefractive single crystal, the laser beam is destroyed and its polarization is disrupted due to a change in the refractive indices, which significantly depend on the magnitude of the photorefraction effect [6, 7, 26]. This fact makes it possible to simultaneously study the state of defects, compositional homogeneity, and photorefractive properties of the crystal from Raman spectra.

An essential feature of all nonstoichiometric $LiNbO_3$ crystals is the presence in the Raman spectra of low-intensity 'extra' lines that do not correspond to fundamental vibrations of the crystal lattice and are not provided for by the selection rules for the space group C_{3V}^6 ($R3c$), which characterizes the symmetry of its unit cell with two formula units. Moreover, in the Raman spectrum of $LiNbO_3$ crystals of strictly stoichiometric composition ($R = [Li]/[Nb] = 1$), 'extra' lines are absent. This fact is important for physical materials science and the technology of obtaining single crystals, since it allows one to evaluate the stoichiometry, the state of defects, and the compositional homogeneity of single crystals by the intensity of the 'extra' lines. Data on the state of defects and compositional homogeneity of photorefractive $LiNbO_3$ crystals of different compositions and manufacturing technologies obtained by Raman spectroscopy are especially informa-

tive in combination with data from laser conoscopy, photoinduced light scattering (PILS), optical spectroscopy, and X-ray diffraction analysis [26, 27, 33–36, 43–46]. Laser conoscopy allows one to observe large-scale (greater than 0.5 m) conoscopic patterns of very high quality, significant aperture, and high contrast and resolution on a screen, and to process them mathematically [47, 48]. The significant image size allows a detailed analysis to be performed of fine features of structural distortions in crystals, both at the center of the field of view and in the peripheral areas of conoscopic patterns. Laser conoscopy acquires special information when studying fine structural distortions, both intrinsic and those induced by laser radiation, in photorefractive crystals. Photoinduced light scattering (scattering of coherent laser radiation by photoinduced small-scale structural extended defects whose refractive indices differ from those of the crystal matrix) is a consequence of the photorefractive effect. Full-profile X-ray diffraction analysis (Rietveld method) allows studying the features of structural distortions in a crystal that arise when its composition alters due to changes in the bond lengths between crystal atoms and changes in the order of cations and point defects along the polar axis. When the O–O, *Me*–O (*Me* = Li, Nb, alloying element) bond lengths change in an $LiNbO_3$ crystal, the conformation changes of the oxygen-octahedral Me_6 clusters of the structure, which are responsible for the ferroelectric and nonlinear optical properties of the crystal [26, 27, 33–36, 45, 46].

The present work reviews studies which were performed using the methods of Raman spectroscopy, laser conoscopy, and photoinduced light scattering of the influence of point defects of the cation sublattice, as well as of extended structural inhomogeneities of various types present in $LiNbO_3$ crystals single and double doped with nonphotorefractive and photorefractive elements. In doing this, we placed emphasis on the manifestation in the Raman spectra of low-intensity 'extra' lines that do not correspond to fundamental vibrations of the crystal lattice. The results of the studies were compared with those obtained for nominally pure crystals of stoichiometric ($LiNbO_{3\,stoich.}$) and congruent compositions ($LiNbO_{3\,congr.}$), which enjoy wide use in industry for the manufacture of functional optical elements for various purposes. Previously, the literature mainly focused on studies devoted to the effect of Fe and Rh photorefractive metals on the properties of $LiNbO_3$ crystals (reviews are given in Refs [7, 8, 49]). The effect of Cu photorefractive metal on the physical characteristics of $LiNbO_3$ crystals has not been studied to date; there are only a few publications [13, 14]. Crystals with low (up to the first density threshold) metal dopant density discussed in this paper are promising as materials for nonlinear optical conversion and modulation of laser radiation [2, 6, 7, 10, 12, 16, 17]. In this regard, it is relevant to analyze studies of the fine features of the structure and the state of defects of crystals with a subthreshold density of metal dopants as the most structurally and optically perfect materials for radiation conversion. It is also important to note that, at subthreshold densities of metal dopants, the technological modes of growing single crystals of high compositional homogeneity are close to the modes already developed for nominally pure crystals. That is, single crystals can be grown using technologies developed for nominally pure crystals, which is important from an economic point of view. Therefore, doping of congruent $LiNbO_3$ single crystals by subthreshold metal density has advantages for obtaining single crystals of high optical quality and high compositional homogeneity. The crystals with low (up to the first density threshold) metal dopant density discussed in this paper are promising as materials for nonlinear optical conversion and modulation of laser radiation. In this case, doping with 'nonphotorefractive' metals Zn, Gd entails a significant decrease in the coercive field (up to 1.5 kV mm^{-1}) and the photorefraction effect [6–8, 26, 27, 50], which is important for producing nonlinear optical materials for converting and modulating laser radiation on periodically polarized domain structures.

2. Features of single crystal production technologies and experimental setups for studying their defect state

The growth of $LiNbO_3$ single crystals of different compositions discussed in this paper was performed in the (001) direction by the Czochralski method on a Crystal-2 industrial growth setup equipped with an automatic weighing system for the crystal diameter, which makes it possible to maintain constant conditions during the crystallization of different samples and grow them with fairly reproducible characteristics using a single technology with a vertical movement speed of 1.1 mm h^{-1} and a rotation speed of 14 rpm^{-1}. The choice of such a low growth rate was due to the small axial temperature gradient of ≈ 1 deg mm^{-1}. The constant value of the axial temperature gradient was achieved by a special design of the thermal unit [27]. The constancy of the temperature gradient made it possible to reduce the probability of random temperature fluctuations at the crystal-melt interphase boundary. In order to obtain a highly homogeneous melt, remove gas inclusions, and destroy associative bonds in the melt, the melt was overheated (≈ 380 K) before seeding. Seeding (i.e., bringing the seed into contact with the melt surface) was carried out 5–7 hours after melt production. The density of doping elements in the crystal was determined by atomic emission spectrometry (ICPS-9000 from Shimadzu). To grow single crystals, we used a granulated batch of congruent composition (48.6 mol% Li_2O) developed by us, which was obtained by the synthesis-granulation technique [51].

We performed direct solid-phase doping of crystals. The heart of the direct solid-phase doping technique is the solid-phase synthesis of a mixture of niobium pentoxide, lithium carbonate, and doping element oxide, with subsequent production of a granulated batch during calcination of the mixture in the pre-melting temperature range (1240–1250 °C). Nominally pure $LiNbO_3$ crystals of stoichiometric composition were grown from a melt with 58.6 mol% of Li_2O. The preparation of single crystals is described in detail in Refs [6, 27, 52, 53]. The density of trace amounts of foreign metal impurities in the batch and in the single crystals under study is given in Table 1.

One can see from Table 1 that the crystals are highly homogeneous along the growth axis in terms of the composition of impurities and main components. The Curie temperatures of the cone and end of each single-crystal boule of a certain composition also coincide within the experimental errors, which confirms the high homogeneity of the composition of the grown crystals.

All grown $LiNbO_3$ single crystals were subjected to thermal and electrothermal treatment [27]. Post-growth annealing of the crystal consisted of long-lasting (for ≈ 2 h) holding of the crystal boule above the melt and subsequent cooling of the thermal unit at a rate of 50 deg h^{-1}. The final removal of the

Table 1. Impurity composition (C, wt.%) of granulated lithium niobate batch, as well as of conical and end parts of $LiNbO_3$:*Me* (*Me* = Zn, Cu, Gd) single crystals under study [27, 51].

Impurity elements		Mn	Ni	Al	Fe	Cr, Cu, V	Pb, Sn	Bi	Mg	Si, Ti, Mo, Ca, Co	Sb	Zr
$C \times 10^{-3}$, wt.%	Batch	< 0.2	< 0.3	< 0.3	< 0.3	0.3	< 0.5	0.5	0.5	1	2.1	< 10
	Crystal cone	< 0.2	< 0.3	< 0.3	0.32	0.3	< 0.5	0.5	0.53	1	1.7	10
	Crystal end	< 0.2	< 0.3	1	0.38	0.3	< 0.5	0.5	0.58	1	2	10

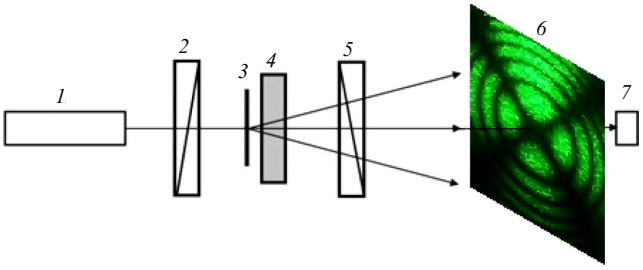

Figure 2. Schematic diagram of experimental setup for laser conoscopy: *1* — YAG:Nd MLL-100 yttrium-aluminum garnet laser; *2* — polarizer; *3* — scatterer; *4* — sample; *5* — analyzer; *6* — semi-transparent screen; *7* — digital camera [47].

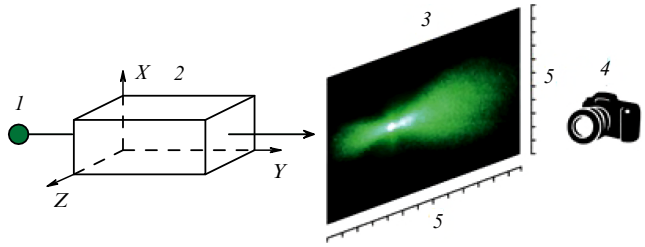

Figure 3. Schematic diagram of experimental setup for studying photo-induced light scattering: *1* — YAG:Nd MLL-100 laser; *2* — crystal; *3* — semi-transparent screen; *4* — video camera; *5* — ruler [47].

crystal was performed only after complete cooling of the crystallization unit to room temperature approximately 12 hours after switching off the setup. The crystals were single-domained on the Lantan apparatus by the method of high-temperature electrodiffusion annealing with cooling of the samples at a rate of 20 deg h^{-1} in the temperature range of $\sim$ 1515–1165 K under the conditions of applied electric voltage. The degree of single-domaining of the crystals was controlled by analyzing the frequency dependence of electrical impedance and by determining the value of the static piezoelectric modulus ($d_{333\,st.}$) of the crystal boule.

Samples for studies by Raman spectroscopy, PILS, and laser conoscopy were cut from single-domain $LiNbO_3$ crystals either in the form of 1- and 3-mm-thick plates or in the form of rectangular parallelepipeds (dimensions: $\sim 6 \times 5 \times 4$ mm^3), whose edges coincided in direction with the crystallophysical axes X, Y, Z (Z is the polar axis of the crystal). The faces of the parallelepipeds were carefully polished.

The Raman spectra were excited by the 514.5-nm line of a Spectra Physics argon laser (2018-*RM* model) and recorded with a Horiba Jobin Yvon T64000 spectrograph using a confocal microscope in the backscattering geometry and in 90-degree scattering geometries employing a Raman or-*U*1000 spectrometer. The spectra were processed using the Horiba LabSpec 5.0 and Origin 8.1 software packages. The accuracy of line frequency determination was ± 1 cm^{-1}.

The setups for laser conoscopy and PILS are schematized in Figs 2 and 3. The conoscopic experiment was performed with a setup consisting of a polarizer, a diffuser, the single crystal under study, and an analyzer (see Fig. 2). In the experiments, the laser beam axis coincided with the optical axis of the single crystal and was perpendicular to its input face. The transmission axes of the polarizer and analyzer were perpendicular to each other, the transmission axis of the polarizer making an angle of 45° with the vertical. The experiments used radiation from an MLL-100 laser ($\lambda = 532$ nm) with an output power of 1 mW in order to rule out the influence of the photorefractive effect on the conoscopic patterns.

To study the compositional homogeneity and microinclusions of microquantities of impurity phases of other lithium niobates (in addition to lithium metaniobate $LiNbO_3$) in $LiNbO_3$ single crystals using Raman spectroscopy, PILS, and laser conoscopy, the sample under study in the form of a single-crystal plate was placed on a two-coordinate translation stage. By scanning its input face with a laser beam, the two-coordinate translation stage allows one to obtain a series of Raman spectra, conoscopic patterns, and PILS patterns corresponding to different points of the cross section of the sample under study.

The compositional homogeneity in terms of the main components was also controlled by the Curie temperature (T_C) measured by differential thermal analysis (DTA) for plates cut from the top and bottom of single-crystal boules.

3. Features of defect structure of $LiNbO_3$ crystal as a nonstoichiometric phase of variable composition

The $LiNbO_3$ single crystal has a pseudoilmenite structure consisting of six planar rows of oxygen atoms in a distorted hexagonal structure with the closest packing [23] (Fig. 4). Chains of slightly distorted O_6 oxygen octahedra, connected by faces and edges, are extended along the polar Z axis of the crystal. In the polar ferroelectric phase, the Li and Nb ions are shifted along the Z axis relative to the oxygen plane. In the $LiNbO_3$ crystal structure, 1/3 of the O_6 oxygen octahedra is filled with Li^+ ions, 1/3 is filled with Nb^{5+} ions, and 1/3 remains unoccupied (vacant) [20, 21, 23]. Therefore, the structure of the ferroelectric $LiNbO_3$ crystal along the direction of the polar axis Z can be represented as an Li–Nb-vacancy . . . Li–Nb-vacancy chain. The distribution of cations over octahedra along the polar axis depends heavily on the composition and crystal production technology, and determines the ferroelectric properties of the crystal and the state of defectiveness of the cation sublattice along the polar axis [7, 8, 20, 21, 24, 29, 54]. The distribution of the main and impurity cations over the octahedra and the structural disorder in the crystal caused by the presence of point defects in the structure of $LiNbO_3$ crystals of any composition, both

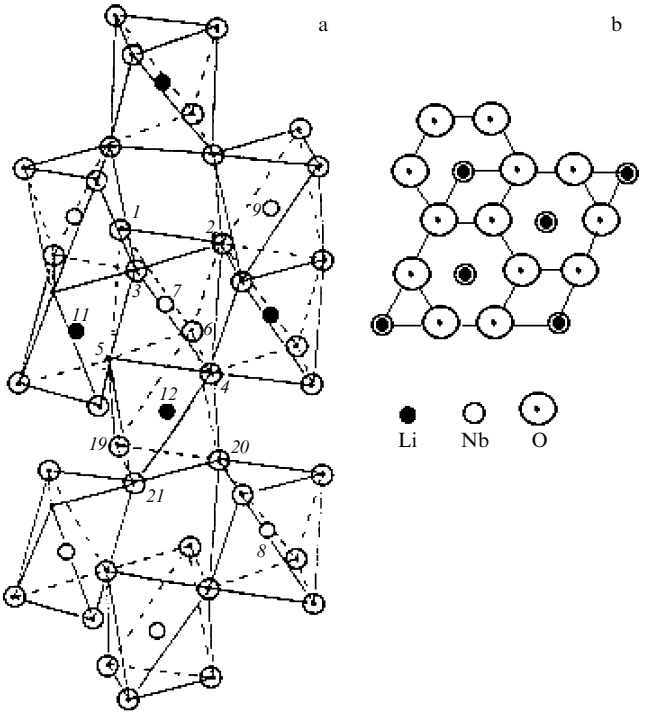

Figure 4. (a) Part of $LiNbO_3$ crystal structure. Columns of oxygen octahedra connected by edges and faces are extended along polar axis. (b) Projection of crystal structure onto [0001] plane [23].

nominally pure (with different ratios $R = [Li]/[Nb]$) and doped, can be modeled using vacancy split models and data from full-profile (Rietveld method) X-ray diffraction analysis [33–35]. The lithium octahedron O_6 in the structure of the $LiNbO_3$ crystal is larger than the niobium and vacant octahedra. This fact qualitatively explains the preferential incorporation of doping metals into the lithium octahedron at their low densities. The congruent melting composition of the $LiNbO_{3congr.}$ crystal corresponds to the ratio $R = [Li]/[Nb] \approx 0.946$ [6, 7]. So, a crystal of congruent composition is characterized by a lithium deficiency of 5.0 mol% Li_2O, i.e., it initially contains a significant amount of point Nb_{Li} defects.

The defect state of an $LiNbO_3$ crystal of any composition depends on the conditions of its growth and thermal prehistory. Cooling of the grown $LiNbO_3$ single crystal to room temperature is usually carried out at a rate of ≈ 50 deg h^{-1}. That is, cooling occurs under substantially nonequilibrium conditions, which, in combination with a strong narrowing of the homogeneity region of the $LiNbO_3$ phase on the $Li_2O - Nb_2O_5$ phase diagram with a decrease in temperature [22] (see Fig. 1), stimulates the appearance of many structural defects of various types in the crystal, both point-like and extended [6, 7, 20, 27, 28]. The most important defects that affect the physical characteristics of the $LiNbO_3$ crystal also include those in the form of OH hydroxyl groups [5, 6, 8]. In addition, the grown $LiNbO_3$ single crystal is characterized by a developed polydomain structure and a high density ($10^{-3} - 10^{-4}$ wt.%) of uncontrolled trace amounts of numerous metal impurities (see Table 1). Since the ferroelectric $LiNbO_3$ crystal of any composition exhibits a photorefraction effect, many nonequilibrium photoinduced defects also appear in a crystal exposed to laser radiation, which disappear upon increasing the temperature to ≈ 320 K [7, 8, 47, 49, 50, 52].

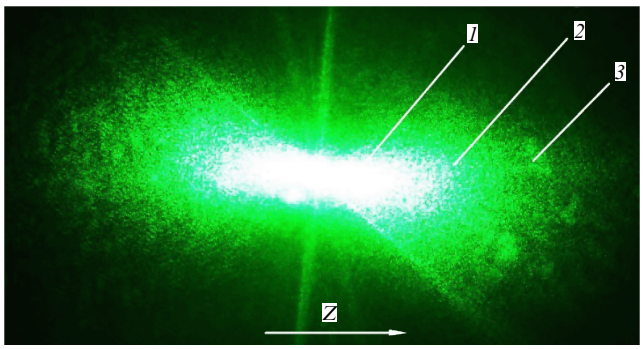

Figure 5. Disruption of laser beam and three-layer PILS speckle structure in an $LiNbO_{3\,stoich.}$ single crystal [47]: *1* — central layer (laser beam); *2* — second layer; *3* — third layer.

4. Evaluation of optical homogeneity and photorefractive properties of $LiNbO_3$ single crystals

The optical homogeneity and photorefractive properties of crystals were evaluated using laser conoscopy and photoinduced light scattering [47]. When laser radiation passes through a photorefractive $LiNbO_3$ crystal, strong destruction of the laser beam and photoinduced light scattering are observed for crystals of some compositions (Figs 5, 6). The PILS indicatrix has the form of an ellipse or figure eight and three layers with a clearly pronounced granular structure (speckle structure), and its opening occurs mainly in the direction of the polar axis Z (see Fig. 5). In this case, a complex pattern of intensity minima and maxima (speckle pattern) is formed, whose appearance is determined by the structure of the crystal, the features of its defect structure, and the magnitude of the photorefraction effect [47].

The temporal dependences of the PILS patterns obtained at an exciting laser radiation intensity of 6.3 W cm^{-2} are plotted in Fig. 6. For $LiNbO_{3\,congr.}$, $LiNbO_3$:Gd (0.002, 0.44 wt.%), $LiNbO_3$:Zn (1.98, 2.05 wt.%) crystals, the PILS patterns remain virtually unchanged with time, there is no photorefractive response, and only circular scattering from static structural defects is observed. The scattering pattern retains a shape close to a circle throughout the experiment (see Fig. 6 (*2–6*)). The PILS patterns of $LiNbO_{3\,stoich.}$, $LiNbO_3$:Cu(0.34):Gd (0.06 wt.%), $LiNbO_3$:Cu(0.37):Gd (0.07 wt.%) crystals (see Fig. 6 (*1*, *7*, *8*)) change significantly in time: they are first transformed into an oval ('comet-like') shape, and then assume the appearance of an asymmetric figure eight oriented along the polar axis of the crystal. The PILS indicatrix unfolds very quickly, practically within the first second of laser irradiation of the crystal (see Fig. 6 (*1*, *7*, *8*)). The opening of the PILS indicatrix indicates the presence of a photorefractive effect in lithium niobate single crystals of stoichiometric composition, $LiNbO_3$:Cu(0.34):Gd (0.06 wt.%), $LiNbO_3$:Cu(0.37):Gd(0.07 wt.%).

The conoscopic patterns of the crystals under study are shown in Fig. 7. As is well known [7, 47], the stoichiometric $LiNbO_{3stoich.}$ crystal grown from a melt with a significant excess of lithium (58.6 mol% Li_2O) is characterized by significant nonuniformity of the refractive index along the growth axis. For this reason, the conoscopic patterns of the $LiNbO_3$ stoichiometric crystal are strongly blurred (see Fig. 7 (*1*)). For the other crystals under study, both in the conoscopic patterns and in the PILS patterns, noticeable

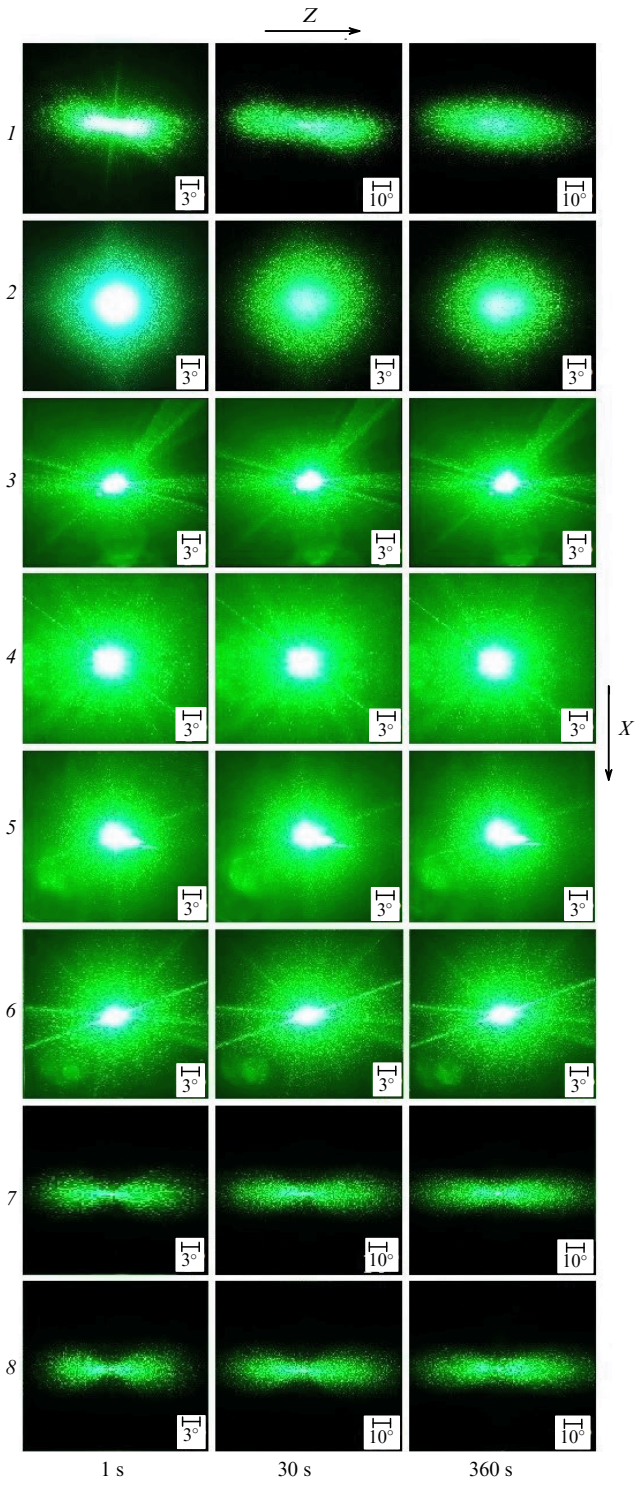

Figure 6. PILS patterns of $LiNbO_3$ crystals of different compositions: *1* — $LiNbO_{3\,stoich.}$; *2* — $LiNbO_{3\,congr.}$; *3* — $LiNbO_3$3:Gd (0.002 wt.%); *4* — $LiNbO_3$:Gd (0.44 wt.%); *5* — $LiNbO_3$:Zn (1.98 wt.%); *6* — $LiNbO_3$:Zn (2.05 wt.%); *7* — $LiNbO_3$:Cu (0.34):Gd (0.06 wt.%); *8* — $LiNbO_3$:Cu (0.37):Gd (0.07 wt.%). $P = 6.3$ W cm^{-2}. PILS patterns of $LiNbO_{3\,stoich.}$, $LiNbO_{3\,congr.}$, $LiNbO_3$:Gd (0.002 wt.%), and $LiNbO_3$:Zn (1.98 wt.%) crystals were first described in detail in Ref. [47]. PILS patterns of $LiNbO_3$:Gd (0.44 wt.%), $LiNbO_3$:Zn (2.05 wt.%), $LiNbO_3$:Cu (0.34):Gd (0.06 wt.%), and $LiNbO_3$:Cu (0.37):Gd (0.07 wt.%) crystals had not been previously studied and are presented in this review for the first time.

differences were found, depending on the composition of the crystal. One can see from Fig. 7 (*2*, *3*) that the $LiNbO_{3\,congr.}$ and $LiNbO_3$:Gd(0.002 wt.%) crystals are characterized by

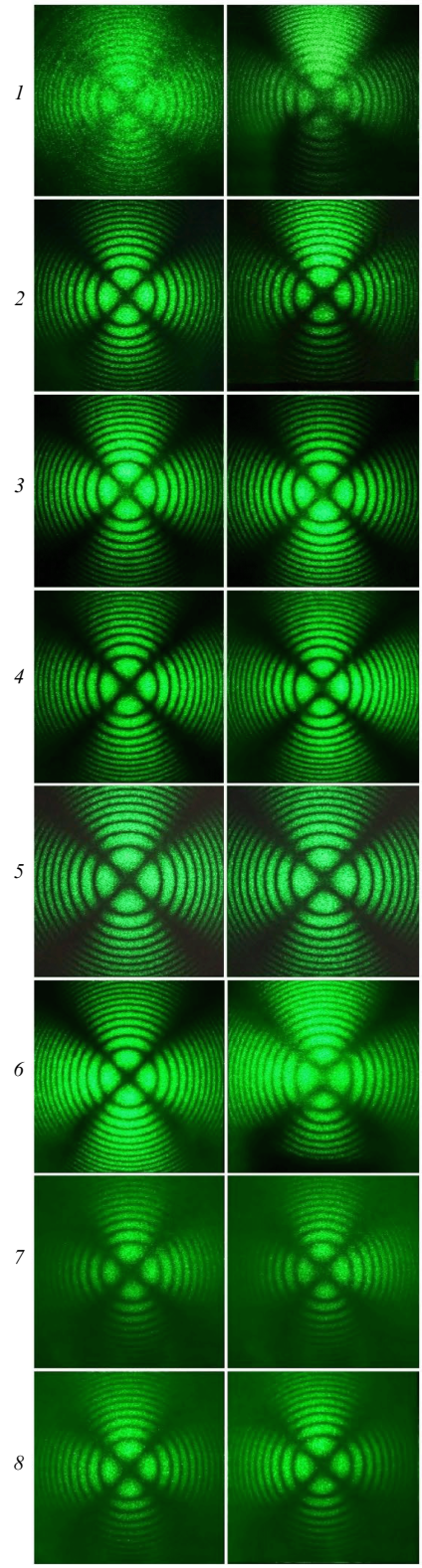

Figure 7. Conoscopic patterns of $LiNbO_3$ crystals of different compositions [47]: *1* — $LiNbO_{3\,stoich.}$; *2* — $LiNbO_{3\,congr.}$; *3* — $LiNbO_3$:Gd (0.002 wt.%); *4* — $LiNbO_3$:Gd (0.44 wt.%); *5* — $LiNbO_3$:Zn (1.98 wt.%); *6* — $LiNbO_3$:Zn (2.05 wt.%); *7* — $LiNbO_3$:Cu (0.34):Gd (0.06 wt.%); *8* — $LiNbO_3$:Cu (0.37):Gd (0.07 wt.%). $P = 1$ mW. PILS patterns of $LiNbO_{3\,stoich.}$, $LiNbO_{3\,congr.}$, $LiNbO_3$:Gd (0.002 wt.%), and $LiNbO_3$:Zn (1.98 wt.%) crystals were first described in detail in Ref. [47]. Conoscopic patterns of $LiNbO_3$:Gd (0.44 wt.%), $LiNbO_3$:Zn (2.05 wt.%), $LiNbO_3$:Cu (0.34):Gd (0.06 wt.%), and $LiNbO_3$:Cu(0.37):Gd (0.07 wt.%) crystals had not been previously studied and are presented in this review for the first time.

high optical homogeneity: in scanning along the plane of the input faces, practically identical conoscopic patterns are observed, which correspond to a high-perfection optically uniaxial crystal. At the same time, for heavily doped crystals with single and double doping $LiNbO_3$:Gd (0.44 wt.%), $LiNbO_3$:Zn (1.98, 2.05 wt.%), $LiNbO_3$:Cu(0.34):Gd (0.06 wt.%), $LiNbO_3$:Cu(0.37):Gd (0.07 wt.%), when scanning along the plane of the input face, two types of conoscopic patterns were obtained (see Fig. 6 (*4–8*)), corresponding to both an optically homogeneous crystal and a crystal with indications of anomalous optical biaxiality: the 'Maltese cross' is deformed, the circular symmetry of the conoscopic pattern is broken, and the isochromes acquire the form of ellipses. The appearance of weak anomalous optical biaxiality in the conoscopic patterns of heavily doped crystals may be due to local distortions of the crystal structure, whose nature is being little studied at present and calls for careful examination. Local distortions of the crystal structure that arise at high gradients of dopant densities may lead to the appearance of growth bands in the crystal [6, 27, 28]. The occurrence of growth bands is accompanied by the appearance of microdefects in the form of dislocations, microdomains, domain boundaries, and a block structure, especially in the region of enhanced gradients of dopant densities at the boundaries of growth bands. Accumulations of microdefects will inevitably lead to a local change in the elastic characteristics of the crystal and the appearance of mechanical stresses that locally distort the optical indicatrix of a uniaxial crystal and affect its nonlinear optical characteristics [6, 25–32, 43, 47, 49]. One of the reasons for the appearance of optical heterogeneity of both nominally pure and doped crystals may also be the presence in their structure of microstructures (clusters) of various types, whose structure differs from that of the crystalline matrix. Such microstructures can be detected from Raman spectra [6, 7, 25, 26, 52, 54].

5. Raman spectra of nonstoichiometric $LiNbO_3$ crystals

The Raman spectra of $LiNbO_3$ crystals of different compositions and production technologies have been studied in detail in the frequency range of 10–1000 cm^{-1} for many years [6, 7, 25, 26, 52, 54, 56–70]. Early studies of Raman spectra recorded in the frequency range of 10–1000 cm^{-1} are reviewed in Refs [7, 26, 54, 56, 66–69]. The rhombohedral unit cell of the ferroelectric phase of the $LiNbO_3$ crystal is characterized by the space symmetry group C_{3V}^6 ($R3c$) and contains two formula units [21, 23]. The unit cell contains 10 atoms, i.e., 30 degrees of freedom. The phonon dispersion curve thus has 30 vibrational branches, of which 27 are optical and 3 are acoustic [7]. The Raman tensors for irreducible representations of the symmetry group C_{3V}^6 have the form [7]

$$A_1(Z)=\begin{pmatrix} a & 0 & 0\\ 0 & a & 0\\ 0 & 0 & b\end{pmatrix},\quad E(X)=\begin{pmatrix} 0 & c & d\\ c & 0 & 0\\ d & 0 & 0\end{pmatrix},$$

$$E(Y)=\begin{pmatrix} c & 0 & 0\\ 0 & -c & d\\ 0 & d & 0\end{pmatrix}.$$

According to the irreducible representation of the space group C_{3V}^6, the distribution in symmetry of vibrations at the center of the Brillouin zone is of the form [7]

$$5A_1(Z)+5A_2+10E(X,Y).$$

Of these, $1A_1(Z)+1E(X,Y)$ fundamental vibrations are acoustic and the remaining $4A_1(Z)+5A_2+9E(X,Y)$ are optical [7]. $4A_1(Z)+9E(X,Y)$ optical fundamental vibrations are dipole, active in both Raman and IR absorption spectra. Fundamental vibrations of A_2 symmetry are pseudoscalar (they do not change the dipole moment of the unit cell) and are not active in Raman and IR absorption spectra. The absence of an inversion center in the space group of the symmetry of the unit cell of the $LiNbO_3$ crystal leads to the appearance of a dipole moment, and the macroscopic electric field splits each dipole-active vibration into longitudinal (LO) and transverse (TO) [55]. Therefore, in the polarized radiation in the Raman spectra of the $LiNbO_3$ single crystal, in the phonon propagation along the main crystallographic axes X, Y, Z, and taking into account the LO–TO splitting, 26 fundamental vibrations should appear in the corresponding scattering geometries. In the Raman spectrum of the LO–TO polycrystal, the splitting of vibrations is nonexistent, and only 13 fundamental vibrations should manifest themselves. It follows from the form of the Raman tensors that, in the Raman spectrum in the (ZZ) polarization, only nondegenerate vibrations of the $A_1(\mathrm{TO})$ symmetry type appear. In the (XY), (XZ), (YX), (YZ), (ZX), and (ZY) polarizations, the spectrum should contain only doubly degenerate $E(\mathrm{TO})$ symmetry vibrations. In the (XX) polarization, the spectrum should simultaneously contain $A_1(\mathrm{TO})+E(\mathrm{LO})$ symmetry vibrations. In the (YY) polarization, the spectrum should simultaneously contain $A_1(\mathrm{TO})+E(\mathrm{TO})$ symmetry vibrations. It is important to note that there are no polarization scattering geometries in which only vibrations of the $A_1(\mathrm{LO})$ symmetry type or only vibrations of the $E(\mathrm{LO})$ symmetry type would appear in the Raman spectrum of the $LiNbO_3$ crystal.

It is noteworthy that the manifestation of purely TO and purely LO fundamental vibrations in the Raman spectra in polarized radiation is possible only for ideal $LiNbO_3$ single crystals, where the photorefraction effect is zero, and only when the wave vector of the **k** vibration is strictly parallel ($\theta = 0°$) or strictly perpendicular ($\theta = 90°$) to the polar axis Z of the crystal [7, 65]. In this case, the crystal is free of the effects of interaction of long-range electrostatic forces that cause LO–TO splitting of polar vibrations and short-range elastic forces due to the anisotropy of the crystal [55]. With an arbitrary orientation of the wave vector of the **k** vibration ($0 < \theta < 1$) relative to the polar axis, all polar vibrations in the $LiNbO_3$ crystal are coupled to each other by long-range electrostatic forces and are of a mixed nature [55]. The frequencies of mixed fundamental vibrations depend on the angle θ and have an intermediate value between the frequencies of pure LO and pure TO vibrations. The dependences of the frequency of mixed vibrations on the angle θ between the wave vector **k** and the Z axis ($0 < \theta < 0$) were studied in Refs [7, 65–69]. As shown in these studies, the following types of mixed vibrations can appear in the Raman spectra of the $LiNbO_3$ crystal at $0 < \theta < 1$: longitudinal-transverse mixed vibrations with polarization parallel to the Z axis ($A_1(\mathrm{TO})+A_1(\mathrm{LO})$) and with polarization perpendicular to the Z axis ($E(\mathrm{TO})+E(\mathrm{LO})$); quasi-transverse vibrations ($E(\mathrm{TO})+A_1(\mathrm{TO})$), whose polarization is perpendicular to the wave vector **k**; and quasi-longitudinal vibrations ($E(\mathrm{LO})+A_1(\mathrm{LO})$), whose polarization is parallel to the wave vector **k**. The change in the frequency of mixed vibrations of the $LiNbO_3$ crystal for some vibrational branches with an increase in the angle θ is indicated by arrows in Table 2.

Table 2. Types of optical branches of mixed vibrations in $LiNbO_3$ crystal. (Data from Refs [7, 64, 65, 69] were used to fill in the table).

Branch numbers	E-vibrations ν_{TO} ν_{LO}	A_1-vibrations ν_{TO} ν_{LO}	Mixed vibration type
1	155 → 198		LO – TO
2	236 → 243		LO – TO
3	265 →	255	Quasi-transverse $E(TO) + A_1(TO)$
4		276 ← 275	LO – TO
5	325 → 295		LO – TO
6		334 ← 333	LO – TO
7	371 → 371		LO – TO
8	431 → 428		LO – TO
9	454	← 436	Quasi-longitudinal $E(LO) + A_1(LO)$
10	582 →	633	Quasi-transverse $E(TO) + A_1(TO)$
11	880	← 876	Quasi-longitudinal $E(LO) + A_1(LO)$

Therefore, when interpreting the Raman spectra of the $LiNbO_3$ crystal recorded in different polarization scattering geometries, we do well to bear in mind the following. Due to the dependence of the vibration wave vector **k** on its orientation relative to the main crystallographic axes X, Y, Z, some low-intensity lines in the frequency range of 150–900 cm^{-1}, which correspond to mixed fundamental vibrations of the crystal lattice, due to errors in polarization measurements can be erroneously attributed to 'extra' lines that do not correspond to fundamental vibrations of the lattice.

Table 3 presents the frequency values of the experimentally observed lines corresponding to fundamental vibrations of the crystal lattice in the Raman spectra of the congruent $LiNbO_{3\,congr.}$ crystal, which were recorded in different polarization scattering geometries, and gives their classification according to the vibration symmetry types. It also presents the frequencies of the 'extra' lines experimentally detected in Refs [7, 25, 26, 33, 54, 56, 62–69, 71–74] in the same frequency range of 100–900 cm^{-1}, which hosts the fundamental vibrations of the crystal lattice. As is well known [7, 25, 26, 33, 54, 56, 62–69, 71–74], in the Raman spectrum of $LiNbO_{3\,congr.}$ crystals of different compositions and production technologies (except for the spectrum of the stoichiometric $LiNbO_{3\,stoich.}$ crystal), in addition to the lines corresponding to fundamental lattice vibrations, there are low-intensity 'extra' lines with frequencies of 104, 120, 305, 412, 477, 540, 605, 675, 668, 690, 738, 743, 773, 825, 840 cm^{-1}. These 'extra' lines, not observed by all researchers and not for all samples, do not fit into the interpretation of the spectrum within the framework of fundamental lattice vibrations. A significant part of these 'extra' lines have not been attributed to specific scattering processes. Figure 8 shows, by way of example, the Raman spectra of a nominally pure $LiNbO_{3\,congr.}$ crystal; the 'extra' lines observed in the Raman spectra are indicated by arrows.

The lattice dynamics of the $LiNbO_3$ crystal were analyzed by both first-principle (*ab initio*) methods in the WIEN97 FLAPW (Full potential Linear Augmented Plane Wave) and LDA (Local-Density Approximation) approximations [75], in the LCAO (Local Combination Atomic Orbitals) approximation [64], and in the valence-force field approximation [76]. The calculated frequencies of purely transverse (TO) and purely longitudinal (LO) vibrations at the center of the Brillouin zone are collected in Table 3.

As a result of the analysis of numerous studies of Raman spectra performed by different authors for a large number of $LiNbO_3$ single crystals with different compositions, both nominally pure and doped with a wide range of metals, produced by different technologies [6, 7, 25, 26, 33–36, 52, 54, 56–69, 71–73], it is safe to say that experimentally observed in the Raman spectrum of $LiNbO_3$ crystals are seven groups of lines of different origins.

The first group comprises the most intense lines corresponding to fundamental vibrations of the crystal lattice, which show up in the frequency range of 100–900 cm^{-1}. The frequencies of fundamental vibrations of the $A_1(TO)$, $A_1(LO)$, $E(TO)$, $E(LO)$ symmetry type, which appear in the Raman spectrum of the $LiNbO_{3\,stoich.}$ crystal, are given in Tables 2 and 3. The second and third groups of lines consist of 'extra' lines corresponding to fundamental vibrations of the crystal lattice in the frequency range of 100–900 cm^{-1}, which are forbidden in the spectrum in the scattering geometry under study, but appear in this scattering geometry due to the photorefraction effect or polarization measurement errors. The fourth group of lines consists of 'extra' lines corresponding to mixed fundamental vibrations $E(LO\text{-}TO)$, $E(TO) + A_1(TO)$, $E(LO) + A_1(TO)$, $E(LO) + A_1(LO)$, which have frequencies different from those of vibrations of the $E(TO)$, $E(LO)$, $A_1(TO)$, $A_1(LO)$ symmetry types manifested in the Raman spectrum in some specific polarization scattering geometries and also due to polarization measurement errors (see Table 2). The frequencies of mixed vibrations depend significantly on the orientation of the vibration wave vector relative to the main crystallographic axes Y, Z (see Table 2). The fifth group consists of 'extra' lines manifested in various scattering geometries in the same frequency range (100–900 cm^{-1}) as the lines corresponding to the fundamental vibrations of the crystal lattice caused by the structural features of the $LiNbO_3$ crystal as a nonstoichiometric phase of variable composition. These 'extra' lines are almost two orders of magnitude lower in intensity than those corresponding to fundamental vibrations. The number of 'extra' lines of this group in the Raman spectrum depends on the composition, production technology, and thermal history of the crystal. It is comparable to the number of lines corresponding to fundamental lattice vibrations. The nature of such lines is intensely debated in the literature [6, 7, 25, 26, 33–36, 52, 54–69, 71–73], and they are the most difficult to interpret. The sixth group consists of lines caused by the presence in the structure of the $LiNbO_3$ crystal of microregions (clusters), whose structure differs from that of the crystalline matrix. The seventh group of lines comprises low-intensity 'extra' lines that show up in the frequency range of 1000–3000 cm^{-1} and correspond to overtone processes. They were discovered relatively recently (in the last 5 years) in the Raman spectra of nonstoichiometric single crystals (both nominally pure and doped) [57–60, 77, 78]. In the Raman spectra of highly ordered $LiNbO_3$ crystals of a stoichiometric composition, no lines were found in the range of 1000–3000 cm^{-1}.

The nature of the appearance of many 'extra' lines in the Raman spectrum of the $LiNbO_3$ crystal (see Table 3) has not yet been established. The reasons for the appearance of 'extra'

Table 3. Line frequencies (ν, cm^{-1}) in Raman spectrum of $LiNbO_{3\,congr.}$ single crystal, corresponding to fundamental vibrations of the crystal lattice [7]. Experimentally observed (exp.) frequencies of 'extra' lines in region of fundamental vibrations of crystal lattice (100–900 cm^{-1}) [7, 25, 26, 33, 54, 56, 62–69, 71–73] and in region of overtones of fundamental vibrations (1000–2500 cm^{-1}) [57–60], as well as frequencies of fundamental vibrations calculated from first principles (*ab initio*) [74] in LCAO approximation [64] and valence force field approximation [75]. Line frequencies experimentally observed in scattering geometries $X(YY)X$, $Y(XX)Y$, $Z(XX)Z$, $Z(YY)Z$, which correspond to fundamental vibrations of $A_1(TO)$ and $A_1(LO)$ symmetry types and manifest themselves in polarization geometries $Z(XX)Z$ and $Z(YY)Z$, are marked with an asterisk.

Symmetry type of vibration	Scattering geometry	ν, cm^{-1}
$A_1(TO)$, exp.	$X(ZZ)Y$	254 274 333 630
	$Y(ZZ)Y$	254 274 333 630
Simulation [74]		239 320 381 607
'Extra' lines, exp.	$X(ZZ)Y$	104 120 690 825
	$Y(ZZ)Y$	104 120 690 825
$A_1(LO)$, exp.		275 334 433 876
Simulation [74]		309 381 548 831
$E(TO)$	$X(YZ)X$	152 183 237 262 322 368 431 580 610 737
	$X(ZY)X$	152 183 237 262 322 368 431 580 610 737
	$Y(XZ)Y$	152 183 237 262 322 368 431 580 610 737
	$Y(ZX)Y$	152 183 237 262 322 368 431 580 610 737
	$Z(XY)Z$	152 183 237 262 322 368 431 580 610 737
	$Z(YX)Z$	152 183 237 262 322 368 431 580 610 737
Simulation [74]		157 214 269 349 419 423 446 605 690
Simulation [64]		159 240 256 266 280 320 342 352 369 445 588 635 666
$E(LO)$, exp.		204 217 316 372 422 445 570 678 856
Simulation [75]		
$A_1(TO)+E(TO)$	$X(YY)X$	151 183 236 254* 263 275* 322 332* 369 432 578 631* 738
$A_1(TO)+E(LO)$	$Y(XX)Y$	151 183 194 238 254* 275* 295 366 425 456 625 631 880
$A_1(LO)+E(TO)$	$Z(XX)Z$	152 184 236 263 275* 322 369 419 434* 578 737 875*
$A_1(LO)+E(TO)$	$Z(YY)Z$	152 184 236 263 274* 322 369 419 434* 578 737 875*
Simulation [76]	A_1	239 271 329 633
	E	163 200 249 267 324 372 424 572 620
Simulation [64]	$A_1(TO)$	256 280 342 635
	$E(TO)$	159 240 266 320 352 369 445 588 666
A. 'Extra' lines		104, 120, 305, 412, 477, 540, 605, 675, 668, 690, 738, 748, 773, 825, 840
B. 'Extra' lines		1188, 1268, 1326, 1467, 1475, 1482, 1630, 1730, 1761, 1793, 1924, 1932, 2025, 2177, 2331

Note. A. 'Extra' lines of Raman spectrum of $LiNbO_3$ crystals of different compositions, which are observed in Refs [7, 25, 26, 33, 54, 56, 62–69, 71–73] in different scattering geometries in region of fundamental lattice vibration frequencies (100–900 cm^{-1}).
B. 'Extra' lines of Raman spectrum of $LiNbO_3$ crystals of different compositions, which are observed in Refs [57–60] in different scattering geometries in region of overtones of fundamental lattice vibrations (1000–2500 cm^{-1}).

lines in the Raman spectrum of nonstoichiometric $LiNbO_3$ crystals (both nominally pure and doped), in our opinion, lie in the features of the complex defect structure of $LiNbO_3$ crystals as a phase of variable composition with a wide homogeneity region on the phase diagram, which narrows sharply with decreasing temperature (see Fig. 1), in the presence of the photorefraction effect, which entails destruction and depolarization of the laser beam in the crystal (see Fig. 6), in the strong interaction of some fundamental acoustic and optical vibrations with each other, and in the strong interaction of acoustic vibrations with the lowest-frequency optical vibrations. The appearance of some 'extra' lines in the spectrum may also be associated with the specific features of batch and crystal production technologies that affect the state of defects and compositional homogeneity of a single crystal [6, 27]. The specific features of the state of the defect structure and the presence of microstructures in the form of clusters in the crystal structure may have the effect that fundamental vibrations that are optically inactive for the space symmetry group C_{3V}^6 ($R3c$) are active in the vibrational spectrum, which may be due to the fact that intrinsic, impurity, and photo-induced structural defects may result in local violations of the crystal microsymmetry. It is also noteworthy that the frequencies of some experimentally observed 'extra' lines do not depend on the crystal composition, which may indicate a mismatch between such 'extra' lines and the fundamental vibrations of the crystal lattice. In this case, most of the 'extra' lines manifest themselves in polarization scattering geometries in which vibrations of the A_1 symmetry type are active and occur along the polar axis of the crystal [7]. Since the emergence of 'extra' lines in the Raman spectrum depends significantly on the crystal defect state, the intensities of 'extra' lines can be a powerful tool for assessing the structural perfection and controlling the technologies of $LiNbO_3$ single crystals of various compositions.

It has been unambiguously shown theoretically and experimentally that the 'extra' line with a frequency of 120 cm^{-1} ($A_1(TO)$) does not correspond to either the fundamental vibrations of the $A_1(Z)$ and $E(X, Y)$ symmetry type or the pseudoscalar vibrations of the A_2 symmetry type forbidden by the selection rules. It corresponds to vibrations of quasiparticles: two-particle states of acoustic vibrations with a zero total wave vector [7, 26, 54, 62, 63, 72]. In Refs [54, 62, 63, 72], it was shown that the distribution of spectral intensity in the

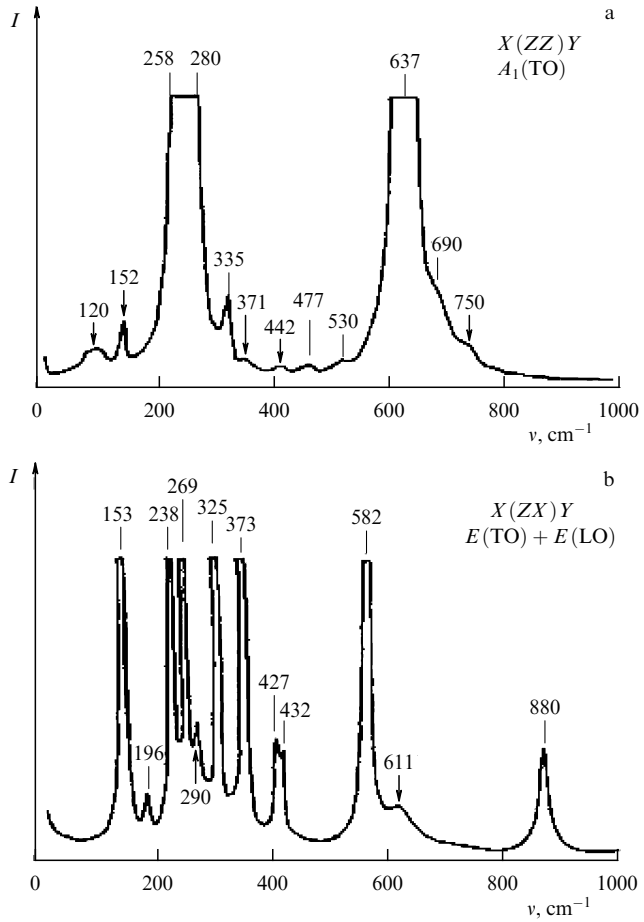

Figure 8. Raman spectra of $LiNbO_{3\,congr.}$ single crystal in scattering geometries $X(ZZ)Y$ (manifested are fundamental vibrations of $A_1(TO)$ symmetry type) and $X(ZX)Y$ (manifested are fundamental vibrations of $E(TO) + E(LO)$ symmetry type). 'Extra' lines observed in this scattering geometry are marked with arrows. $T = 77$ K [7].

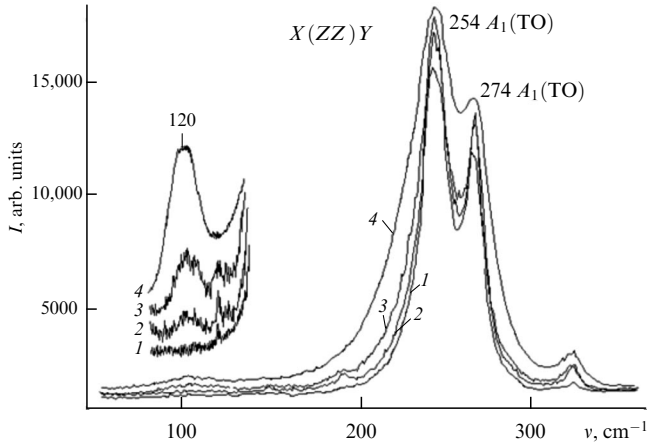

Figure 9. Part of Raman spectrum of lithium niobate single crystals of different compositions in the low-frequency region: *1* — $LiNbO_{3\,stoich.}$; *2* — $LiNbO_{3\,stoich.}$ (6 wt.% K_2O); *3* — $LiNbO_{3\,stoich.}$ (4.5 wt.% K_2O); *4* — $LiNbO_{3\,congr.}$ A decrease in intensity of 120-cm^{-1} frequency line is clearly visible as crystal composition approaches the stoichiometric one [52].

low-frequency region of the Raman spectrum is characteristic of the phonon Fermi resonance. In this case, the manifestation in the Raman spectrum of two-particle acoustic excitations with a zero total wave vector is explained by the effective anharmonic interaction of acoustic vibrations with each other as well as with the lowest-frequency optical vibrations of niobium ions with a frequency of 254 cm^{-1} (quasi-soft mode) and lithium with a frequency of 274 cm^{-1} of the $A_1(TO)$ symmetry type (see Table 3). The nature of the line with a frequency of ≈ 120 cm^{-1} was also discussed in Ref. [61]. The intensity of this line is sensitive to very minor changes in the composition (including the density of Nb_{Li} point defects) and in fine features of the lithium niobate crystal structure [7, 26, 54, 62]. This feature allows the intensity of the line with a frequency of 120 cm^{-1} to be used as a sufficiently accurate experimental criterion for assessing the stoichiometry (the value of $R = [Li]/[Nb]$) of an $LiNbO_3$ single crystal, since, in the Raman spectrum of a nominally pure $LiNbO_{3\,stoich.}$ crystal of strictly stoichiometric composition ($R = 1$), the intensity of the line with a frequency of 120 cm^{-1} is zero [7, 54]. Figure 9 clearly shows a decrease in the intensity of the line with a frequency of 120 cm^{-1} as the composition of a nominally pure $LiNbO_3$ crystal approaches the stoichiometric composition. Therefore, an increase in the value of R of the crystal and, accordingly, the density of Nb_{Li} point defects is accompanied by a decrease in the intensity of the 'extra' line with a frequency of 120 cm^{-1}.

According to the data from X-ray structural analysis and Raman spectroscopy, the value of R can vary significantly and can even be equal to unity, not only in a nominally pure crystal but also when the $LiNbO_3$ crystal is doped with different metals. This occurs due to the substitution of point defects of the Nb_{Li} crystal lattice by the doping metal [26, 27, 33, 34, 79]. The main difference between the defect structures of the cation sublattice of nonstoichiometric $LiNbO_3$ crystals ($R < 1$), both nominally pure and doped, is in the different density of Nb_{Li} point defects and their accompanying compensation point defects V_{Li}, V_{Nb}, etc., as well as in the different order of arrangement of the main (Li and Nb) and doping cations and point defects of different types along the polar axis of the crystal [6–8, 20, 24]. The Nb_{Li} point defect has an effective charge of +4 with respect to the lattice. It is compensated by other point defects; notably, in a pure crystal, the compensation is performed by vacancies (V) in the lithium position (V_{Li}^--defect) [6–8]. In the congruent crystal $LiNbO_{3\,congr.}$ ($R = 0.946$), the density of Nb_{Li} defects is ~ 1 mol% and ~ 4 mol% of V_{Li} point defects. In the structure of the ideal stoichiometric crystal $LiNbO_{3\,stoich.}$ ($R = 1$) there are no Nb_{Li} point defects [5, 7].

A line with a frequency of 120 cm^{-1} of the $A_1(TO)$ symmetry type is not the only 'extra' line in the Raman spectrum, whose intensity lowers with decreasing R. Substitution of Nb_{Li} point defects with a doping metal in the structure of the $LiNbO_3$ crystal also results in a decrease in the intensity of another 'extra' line with a frequency of 737 cm^{-1}. As one can see from Fig. 10 and Table 3, in the spectrum of $LiNbO_{3\,congr.}$, $LiNbO_3$:Gd (0.002 wt.%), $LiNbO_3$:Gd (0.44 wt.%), $LiNbO_3$:Cu(0.37):Gd (0.07 wt.%), $LiNbO_3$:Cu(0.34):Gd (0.06 wt.%) crystals in the polarization scattering geometries $Z(YY)\bar{Z}$, $X(YY)X$, $X(YZ)X$, $X(ZY)X$, $Y(XZ)\bar{Y}$, $Y(ZX)\bar{Y}$, $Z(YX)\bar{Z}$, $Z(XY)\bar{Z}$, $Z(XX)\bar{Z}$ (see Table 3), there is a low-intensity 'extra' line with a frequency of 737 cm^{-1}. At the same time, the low-intensity line with a frequency of 737 cm^{-1} is missing from the spectrum of $LiNbO_{3\,stoich.}$, $LiNbO_3$:Zn (1.98, 2.05 wt.%) crystals (Fig. 10, curves *1*, *5*, *6*).

According to numerous experimental [6, 7, 25, 26, 33, 34, 56–60, 64–69, 71, 73, 74] and simulation [64, 74–76] data, in the Raman spectrum of $LiNbO_3$ crystals of different

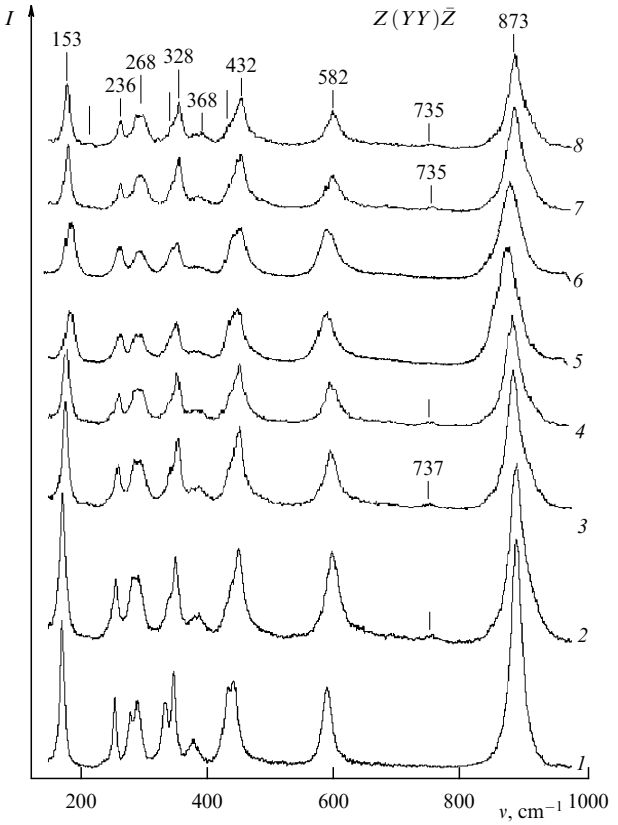

Figure 10. Raman spectra of lithium niobate crystals of different compositions: *1* — $LiNbO_{3\,stoich.}$; *2* — $LiNbO_{3\,congr.}$; *3* — $LiNbO_3$:Gd (0.002 wt.%); *4* — $LiNbO_3$:Gd (0.44 wt.%); *5* — $LiNbO_3$:Zn (1.98 wt.%); *6* — $LiNbO_3$:Zn (2.05 wt.%); *7* — $LiNbO_3$:Cu(0.37):Gd (0.07 wt.%); *8* — $LiNbO_3$:Cu(0.34):Ga (0.06 wt.%). Spectra are published for the first time.

compositions in the frequency range of 700–850 cm^{-1}, there are no lines corresponding to fundamental vibrations of the crystal lattice. Therefore, the low-intensity line with a frequency of 737 cm^{-1}, which appears in polarization scattering geometries in which vibrations of the $E(TO)$, $A_1(TO) + E(TO)$, $A_1(LO) + E(TO)$ symmetry types are active (see Table 3), can be attributed to vibrations of the $E(TO)$ symmetry type. On the other hand, the line with a frequency of 737 cm^{-1} cannot correspond to the fundamental vibration of the $E(TO)$ symmetry type of the $LiNbO_3$ crystal lattice, since all frequencies corresponding to the fundamental vibrations of the $E(TO)$ symmetry type in the Raman spectrum of the congruent $LiNbO_3$ crystal have been experimentally detected and reliably interpreted in the literature (see Table 3) [7, 64, 71, 73–76]. Moreover, it is for the frequencies corresponding to the fundamental vibrations of the $E(TO)$ symmetry type that the best agreement is observed between the experimentally measured frequencies and those calculated from first principles (*ab initio*) (see Table 3). It should also be noted that, according to the data from Refs [74, 80], the line with a frequency of 734 cm^{-1} does not experience a dispersion dependence of the frequency when the angle between the vibration wave vector and the polar axis of the crystal changes from 0 to 90°, but at the same time a change in the polarization of the vibration occurs ($E(TO) \rightarrow E(LO)$).

The following may be responsible for the appearance of an 'extra' line with a frequency of 737 cm^{-1} in the Raman spectrum of nonstoichiometric (both nominally pure and doped) $LiNbO_3$ crystals. First of all, these may be errors in polarization measurements and the photorefraction effect [7, 69, 81]. Polarization measurement errors are excluded immediately in this case, since, in the Raman spectrum of $LiNbO_3$ crystals of different compositions, according to numerous experimental data, there are no other lines in the 700–800-cm^{-1} frequency range, except for a line with a frequency of 737 cm^{-1}. The photorefraction effect is also ruled out, since the line with a frequency of 737 cm^{-1} is present in the spectra of different crystals in the scattering geometries $Z(YY)\bar{Z}$, $Z(YX)\bar{Z}$, $Z(XX)\bar{Z}$, $Y(ZX)\bar{Y}$, both when the spectra are excited by laser radiation in the visible region and when the spectra are excited in the near-IR region ($\lambda_0 = 1064$ nm) [69]. As is well known [7, 8], when a photorefractive crystal is exposed to infrared laser radiation (including the near-IR region), the photorefraction effect does not occur in the $LiNbO_3$ crystal and the Raman spectrum will not exhibit changes due to the photorefraction effect. In the Raman spectrum of $LiNbO_3$ crystals, the photorefraction effect upon excitation in the visible region is most pronounced when it is induced by laser radiation polarized along the polar axis Z, but not along the axis Y, as occurs in the $Z(YY)\bar{Z}$ polarization geometry (see Figs 5, 6). That is, the photorefraction effect is manifested most strongly in the polarization scattering geometries (ZX), (ZY), (ZZ) [7, 47, 49]. In other polarization geometries, the photorefraction effect is much weaker [47, 49]. The destruction of the laser beam in the crystal and the opening of the indicatrix of photoinduced light scattering also occur predominantly along the polar Z axis (see Figs 5, 6).

An essential feature of the $LiNbO_{3\,stoich.}$ crystal and $LiNbO_3$:Zn (1.98, 2.05 wt.%) crystals is that, according to X-ray structural analysis data [45, 46, 82], their structure does not contain Nb_{Li} point defects, which are deep electron traps responsible, according to the data of Ref. [8], for the photorefraction effect. Therefore, it can be assumed that doping of the congruent $LiNbO_3$ crystal ($R = 0.946$) with Zn^{2+} metals increases the stoichiometry of the crystal due to a decrease in the density of Nb_{Li} point defects. However, Fig. 6 shows that, for the $LiNbO_{3\,stoich.}$ crystal, in which there are no Nb_{Li} point defects, the photorefraction effect is observed and the PILS indicatrix opens. At the same time, for the $LiNbO_{3\,congr.}$ crystal, in which the density of Nb_{Li} point defects is highest in the series of crystals under study and is ≈ 1 mol% for the applied laser power density of 6.3 W cm^{-2}, the photorefraction effect is weakest, and no opening of the PILS indicatrix is observed (see Fig. 6). Thus, there are grounds to believe that the absence of Nb_{Li} defects in the structure of $LiNbO_3$ crystals and the photorefraction effect are not related to each other, and the emergence of the 737-cm^{-1} frequency line in the Raman spectrum cannot be due to the photorefraction effect.

The state of the defect structure of the $LiNbO_3$ crystal, as a phase of variable composition, depends on the conditions of its growth and the thermal prehistory of the entire procedure of crystal fabrication [1, 5, 6, 20, 27, 28, 52]. Cooling of the grown $LiNbO_3$ single crystal to room temperature (for the crystals studied in this work, the cooling rate was ≈ 50 deg h^{-1}) took place under significantly nonequilibrium conditions. In combination with a strong narrowing of the homogeneity region of the $LiNbO_3$ phase in the Li_2O–Nb_2O_5 phase diagram with decreasing temperature [7, 22] (see Fig. 1), this fosters the appearance of extended structural defects in

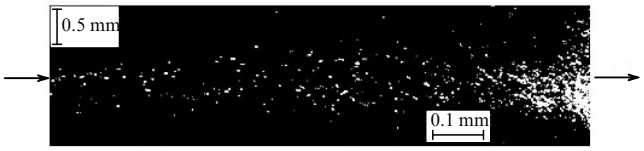

Figure 11. Scattering centers ('sparkles') that appear in $LiNbO_3$ crystal in passage of laser radiation through it. Arrows mark entry to crystal and exit of laser beam from the crystal. Photograph is published for the first time.

the crystal in the form of microstructures (clusters) of various types, as well as the precipitation of microquantities of other lithium niobate phases — $LiNb_3O_8$ and Li_3NbO_4 [7, 52, 83, 84] — into the $LiNbO_3$ matrix. Using an optical microscope, microstructures in the $LiNbO_3$ crystal can be observed visually in the form of scattering centers ('sparkles') of laser radiation passing through the crystal (Fig. 11). Such control is an integral part of the technology of optical $LiNbO_3$ crystals [6, 27]. For $LiNbO_3$ crystals of optical quality, the average density of visually observable microstructures is low and amounts to ≈ 10 cm^{-3} [27].

Microstructures in the form of clusters corresponding to impurity phases can be detected by Raman spectra. Figure 12 depicts the Raman spectra of ceramic samples of pure $LiNbO_{3\,congr.}$, a ceramic sample of $LiNbO_{3\,congr.}$ containing $LiNb_3O_8$ and Li_3NbO_4 phases, as well as the spectra of ceramics of the Li_3NbO_4 and $LiNb_3O_8$ phases. Due to the low density of the $LiNb_3O_8$ and Li_3NbO_4 impurity phases in grown $LiNbO_3$ single crystals, only the most intense lines corresponding to such phases can be observed in the Raman spectrum. Unfortunately, the most intense lines in the Raman spectra of the $LiNb_3O_8$ and Li_3NbO_4 impurity phases are in the same frequency ranges as the lines corresponding to the main phase of $LiNbO_3$ (see Fig. 12). Nevertheless, the $LiNb_3O_8$ and Li_3NbO_4 phases (their Raman spectra are shown in Fig. 12) in the form of microinclusions in the $LiNbO_3$ crystal are confidently detected in the Raman spectra of the $LiNbO_{3\,congr.}$ crystal (see Fig. 12). This is evidenced by the presence of lines with frequencies of 305, 412, 477, 690, 748, 825 cm^{-1} in the Raman spectra of the $LiNb_3O_8$ and Li_3NbO_4 phases and $LiNbO_3$ crystals and ceramics (see Figs 12 and 13) [7]. The presence of microinclusions of the $LiNb_3O_8$ and Li_3NbO_4 impurity phases in the $LiNbO_3$ single crystal is also confirmed by the X-ray topography technique [83, 84].

One can see from Fig. 12 that the lines in the Raman spectrum of the $LiNb_3O_8$ and Li_3NbO_4 ceramic samples are as intense as those in the $LiNbO_3$ spectrum. It is also evident from Fig. 12 that in some cases the spectrum of the congruent ceramic $LiNbO_{3\,congr.}$ subjected to prolonged thermal action at a temperature of 1370 K clearly contains 'extra' lines with frequencies of 540, 675, 690, 748, and 825 cm^{-1}, which correspond to the Raman spectrum of the $LiNb_3O_8$ and Li_3NbO_4 impurity phases. It is significant that the spectrum of the $LiNb_3O_8$ and Li_3NbO_4 impurity phases, which may precipitate during crystallization of $LiNbO_3$, does not contain a line with a frequency of 737 cm^{-1} (see Fig. 12). So, the line with a frequency of 737 cm^{-1}, which manifests itself with confidence in the spectrum of some nonstoichiometric $LiNbO_3$ crystals (see Fig. 10, Table 3), cannot be attributed to the Raman spectrum of the $LiNb_3O_8$ or Li_3NbO_4 impurity phases.

It is noteworthy that, in the Raman spectra of $LiNb_3O_8$, Li_3NbO_4 ceramics, $LiNbO_{3\,congr.}$ ceramics heated at 1500 K,

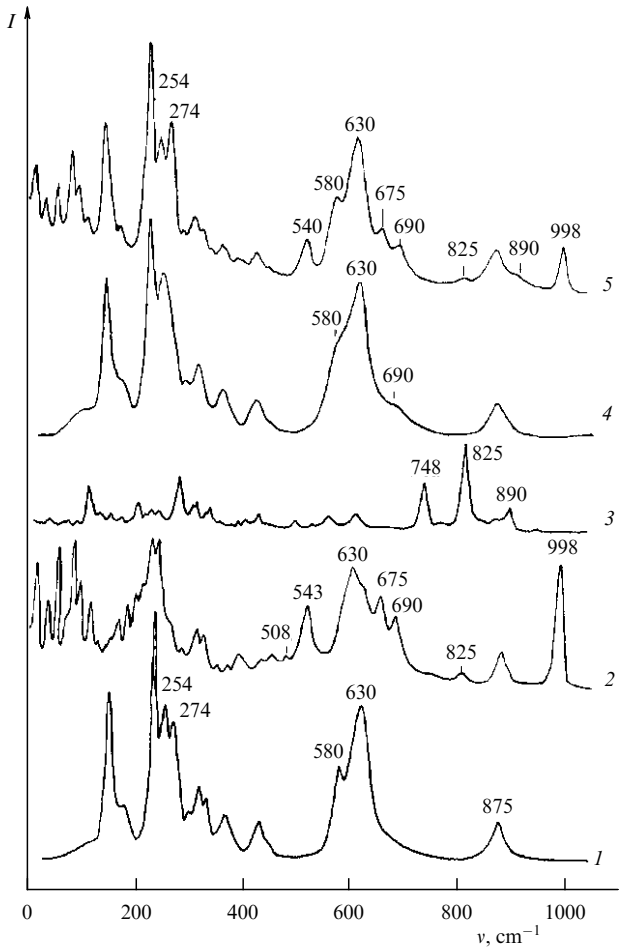

Figure 12. Raman spectra of $LiNbO_3$ ceramic samples recorded at 293 K: *1* — $LiNbO_{3\,congr.}$; *2* — $LiNb_3O_8$; *3* — Li_3NbO_4; *4* — $LiNbO_{3\,congr.}$ heated for 20 h at 1500 K; *5* — $LiNbO_{3\,congr.}$ containing $LiNb_3O_8$ and Li_3NbO_4 phases [7].

and $LiNbO_{3\,congr.}$ ceramics containing $LiNb_3O_8$ and Li_3NbO_4 phases, there is a line with a frequency of 690 cm^{-1} (see Fig. 12), attributed by the authors of Refs [85, 86] to the fundamental lattice vibration of the A_1(TO) symmetry type. Moreover, the intensity of the 690-cm^{-1} frequency line increases slightly as a result of various thermal effects on the crystal (Fig. 13). The most noticeable increase in the intensity of this line is observed in the spectra of single crystals and ceramics with a reduced (compared to the stoichiometric crystal) Li_2O content, where the probability of the formation of lithium-depleted phases is higher [7]. Therefore, the presence of a broad low-intensity line with a frequency of 690 cm^{-1} in the Raman spectrum of the $LiNbO_3$ crystal may be due to the presence of micro-amounts of the $LiNb_3O_8$ phase in its structure. The results obtained convincingly confirm the noticeable influence of the thermal prehistory of the $LiNbO_3$ crystal on the formation of the features of its vibrational spectrum.

Computer simulations of microstructure formation in $LiNbO_3$ crystals of different compositions also suggest that the single crystal grows in clusters [87]. Moreover, an initially formed cluster with any ratio $R = [\mathrm{Li}]/[\mathrm{Nb}]$, including a cluster of stoichiometric composition (at the beginning of its growth), with an increase in the number of atoms in the cluster tends to a cluster of congruent composition ($R = 0.946$). As shown by the method of full-profile X-ray

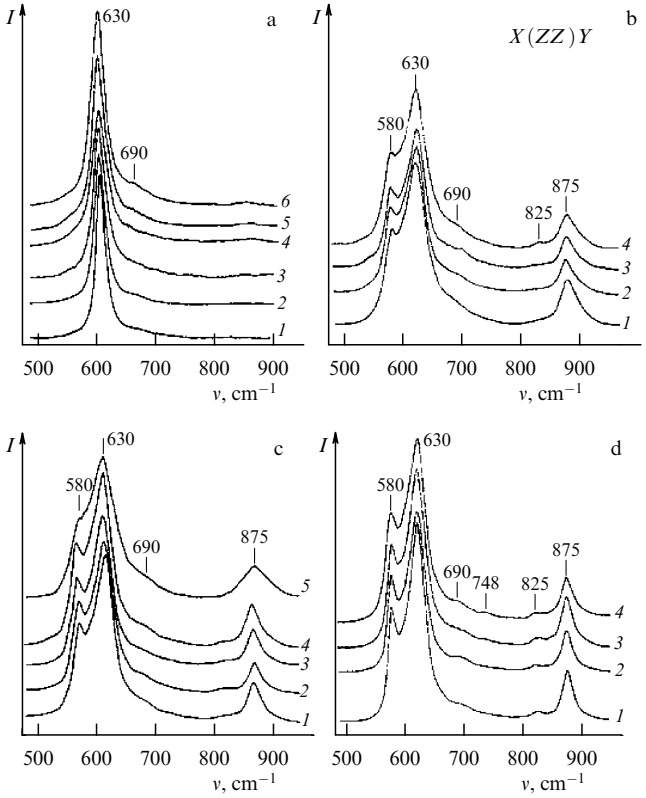

Figure 13. Portions of $LiNbO_3$ Raman spectra ($T = 293$ K) in region of vibration frequencies of oxygen octahedra. Single crystal of $LiNbO_3$ of congruent composition (a) and ceramic samples: with a content of $[Li_2O] = 47.5$ mol% (b), as well as of congruent (c) and stoichiometric (d) compositions after holding for 6 h at 273 K (*1*), 970 (*2*), 1070 (*3*), 1170 (*4*), 1270 (*5*), 1370 K (*6*) [7].

structural analysis (Rietveld method) in Refs [26, 33–35, 45, 46], the 'extra' lines appearing in the X-ray patterns of nonstoichiometric $LiNbO_3$ crystals are caused by the formation in the crystalline matrix of $LiNbO_3$ (space group of symmetry of the unit cell C_{3V}^6 ($R3c$)) of a superstructural ordered hexagonal sublattice of extended defects (clusters). These defects have the structure of ilmenite ($R\bar{3}$ space symmetry group of the unit cell) with a doubled period a of the unit cell in relation to the main cell. In such $LiNbO_3$ clusters with the ilmenite structure, there are Nb_{Li} defects, and the following order of cations and vacancies along the polar axis of the crystal is observed: Nb, Li, □, Li, Nb, □ ... Nb, Li..., which differs from the order of cations in the stoichiometric crystal ($R3c$): Li, Nb, □, Li, Nb, □, Li, Nb, □ ... (□ is a vacant octahedron). The calculated density of Nb_{Li} defects in a congruent cluster with the ilmenite structure is about 5% [35]. The simulations performed in Ref. [34] suggest that the difference in the lattice energy with alternating cations, which are characteristic of the $LiNbO_3$ crystal with the ilmenite structure with the space symmetry group $R\bar{3}$ and the $LiNbO_3$ crystal with the pseudo-ilmenite structure with the space symmetry group $R3c$, is small and amounts to only 0.3%. At the same time, significant differences in the periods of the unit cells are observed for these $LiNbO_3$ structures. The values of the periods for $LiNbO_3$ with the ilmenite structure with the space symmetry group $R\bar{3}$ are $c = 14.35$ Å and $a = 5.21$ Å, and for $LiNbO_3$ with the pseudo-ilmenite structure with the space symmetry group $R3c$ the periods are $c = 13.86$ Å, $a = 5.14$ Å [88]. The possibility of the existence of clusters with the ilmenite structure in nonstoichiometric $LiNbO_3$ crystals is also indicated by data in Refs [33, 36, 70, 88–93]. In particular, a line with a frequency of 738 cm^{-1} was observed in the Raman spectra of $LiNbO_3$:Mg, $LiNbO_3$:Mg:Gd, $LiNbO_3$:In, and $LiNbO_3$:Ti crystals, and its intensity depended on the lithium content in the crystal [36, 93]. At the same time, in the Raman spectrum of some compositions of $LiNbO_3$:Zn crystals, there is no 737-cm^{-1} frequency line (see Fig. 10).

Also noteworthy is the following fact. In Refs [57–60, 77, 78, 94, 95], the Raman spectra of nominally pure congruent $LiNbO_3$ and $LiTaO_3$ crystals, as well as single- and double-doped $LiNbO_3$:Gd(0.003):Mg (0.65 wt.%), $LiNbO_3$:Cu(0.57):Gd (0.76 wt.%), $LiNbO_3$:Gd (0.03–0.26 wt.%), $LiTaO_3$:Cr (0.005 wt.%) crystals, were investigated in a wide frequency range of 50–2500 cm^{-1}. It was shown that some 'extra' lines in the spectrum which were observed in the range above 1000 cm^{-1} belong to the second-order spectrum (overtones) arising from strong anharmonicity of some fundamental vibrations. In this case, observed in the spectrum of the $LiNbO_3$:Gd(0.003):Mg(0.65 wt.%) crystal was a line with a frequency of 1475 cm^{-1} (see Table 3), which may be an overtone of the 737-cm^{-1} frequency line related to the Raman spectrum of microstructures (clusters) in the $LiNbO_3$ crystal but not to the spectrum of the crystalline matrix.

6. Conclusions

The review analyzes the manifestation of 'extra' low-intensity lines in the Raman spectrum of nonstoichiometric $LiNbO_3$ crystals with different compositions, which do not correspond to fundamental vibrations of the crystal lattice, depending on the features of the defect structure. It was found that 'extra' lines are observed in the Raman spectrum of only nonstoichiometric crystals ($R = [Li]/[Nb] < 1$). No 'extra' lines were found in the spectrum of a stoichiometric crystal ($R = 1$), which has the highest-ordered cation sublattice relative to crystals of other compositions. It is shown that there may be several reasons for the emergence of 'extra' lines that do not correspond to fundamental vibrations of the $LiNbO_3$ crystal lattice: the presence of clusters (microstructures) in the crystal matrix, whose structure differs from that of the crystal matrix; the presence of microinclusions of impurity phases of other lithium niobates $LiNb_3O_8$ and Li_3NbO_4; the formation of two-particle states of acoustic phonons active in Raman scattering with the zero total wave vector; and strong anharmonicity of some fundamental vibrations, resulting in the appearance of 'extra' lines corresponding to overtones of fundamental vibrations observed in the range above 1000 cm^{-1}. It was found that the 'extra' line with a frequency of 735–737 cm^{-1} is missing from the Raman spectrum of $LiNbO_{3\,stoich.}$ and $LiNbO_3$:Zn (1.98, 2.05 wt.%) crystals and is present in the spectrum of congruent $LiNbO_{3\,congr.}$ and doped crystals. It is shown that the parameters of the 'extra' lines of the Raman spectrum, which do not correspond to fundamental vibrations of the crystal lattice, can be used as a new highly sensitive and powerful tool for studying the subtle features of the defect state, compositional homogeneity, and structural perfection of $LiNbO_3$ crystals. It is substantiated that the appearance of 'extra' lines in the Raman spectrum can be associated both with the formation of a superstructural ordered defect

sublattice in the lithium niobate crystal structure, which has an ilmenite structure characterized by the space symmetry group $R\bar{3}$, with a doubled (in relation to the crystal matrix) period of a hexagonal elementary cell, and with the existence of clusters in the structure of nonstoichiometric doped crystals, which appear as a result of uneven dopant entry into the crystal. It was determined that doping of the congruent $LiNbO_3$ crystal ($R = 0.946$) increases the stoichiometry of the crystal due to a decrease in the density of Nb_{Li} point defects, according to data in Ref. [8], responsible for the photorefraction effect. It is shown that, in the $LiNbO_{3\,stoich.}$ crystal, in which there are no Nb_{Li} point defects, the photorefraction effect is observed and the PILS indicatrix opens, this opening often being much stronger than in other crystals under study without Nb_{Li} defects. Therefore, there are grounds to believe that the absence of Nb_{Li} point defects, which are deep electron traps, in the structure of $LiNbO_3$ crystals and the photorefraction effect may be unrelated. However, this situation invites careful comprehensive study.

Acknowledgments. The work was performed within the framework of the topic FMEZ-2022-0016.

References

1. Prokhorov A M, Kuz'minov Yu S *Physics and Chemistry of Crystalline Lithium Niobate* (Bristol: Adam Hilger, 1990)
2. Arizmendi L *Phys. Status Solidi A* **201** 253 (2004)
3. Günter P, Huighard J-P (Eds) *Photorefractive Materials and Their Applications 1 Basis Effects* (Springer Series in Optical Sciences, Vol. 113) (New York: Springer, 2006) https://doi.org/10.1007/b106782
4. Kukhtarev N V et al. *J. Appl. Phys.* **106** 014111 (2009)
5. Lúngyel K et al. *Appl. Phys. Rev.* **2** 040601 (2015)
6. Sidorov N V et al. *Monokristally Niobata i Tantalata Litiya Raznogo Sostava i Genezisa* (Single Crystals of Lithium Niobate and Tantalate of Different Composition and Genesis) (Moscow: RAN, 2022)
7. Sidorov N V et al. *Niobat Litiya*: *Defekty, Fotorefraktsiya, Kolebatel'nyi Spektr, Polyaritony* (Lithium Niobate: Defects, Photorefraction, Vibration Spectrum, Polaritons) (Moscow: Nauka, 2003)
8. Volk T, Wöhlecke M *Lithium Niobate. Defects, Photorefraction and Ferroelectric Switching* (Berlin: Springer, 2008)
9. Mkhitaryan N et al. *Eur. Phys. J. Appl. Phys.* **85** 30502 (2019)
10. Chen G et al. *Adv. Photon.* **4** 034003 (2022)
11. Abarkan M et al. *Opt. Mater. Express* **4** 179 (2014)
12. Sánchez-Dena O et al. *Crystals* **10** 990 (2020)
13. Guo Y et al. *Appl. Opt.* **44** 7106 (2005)
14. Wang Y et al. *J. Luminescence* **147** 242 (2014)
15. Blázquez-Castro A, García-Cabañes A, Carrascosa M *Appl. Phys. Rev.* **5** 041101 (2018)
16. Kemlin V et al. *Opt. Express* **21** 28886 (2013)
17. Murray R T et al. *Opt. Express* **25** 6421 (2017)
18. Shur V Ya, Akhmatkhanov A R, Baturin I S *Appl. Phys. Rev.* **2** 040604 (2015)
19. Slautin B N, Zhu H, Shur V Ya *Ferroelecrics* **576** 119 (2021)
20. Abrahams S C, Marsh P *Acta Cryst. B* **42** 61 (1986)
21. Abrahams S C, in *Properties of Lithium Niobate* (EMIS Datareviews Ser., No. 5) (London, New York: INSPEC, Institution of Electrical Engineers, 1989)
22. Svaasand L O et al. *J. Cryst. Growth* **22** 230 (1974)
23. Abrahams S C, Levinstein H J, Reddy J M *J. Phys. Chem. Solids* **27** 1019 (1966)
24. Koyama C et al. *J. Appl. Phys.* **117** 014102 (2015)
25. Fontana M D, Bourson P *Appl. Phys. Rev.* **2** 040602 (2015)
26. Sidorov N, Palatnikov M, Kadetova A *Crystals* **9** 535 (2019)
27. Palatnikov M N et al. *Fundamental'nye Aspekty Tekhnologii Sil'no Legirovannykh Kristallov Niobata Litiya* (Fundamental Aspects of Heavily Doped Lithium Niobate Crystals Technology) (Apatity: KNTs RAN, 2017)
28. Palatnikov M N, Makarova O V, Sidorov N V *Rostovye i Tekhnologicheskie Defekty Kristallov Niobata Litiya Razlichnogo Khimicheskogo Sostava* (Growth and Technological Defects of Lithium Niobate Crystal of Different Chemical Composition) (Apatity: KNTs RAN, 2017)
29. Chen K et al. *Inorg. Chem. Front.* **8** 4006 (2021)
30. Kaczmarek S M, Bodziony T *J. Non-Cryst. Solids* **354** 4202 (2008)
31. Morozov A N et al. *Kristallografiya* **38** (4) 219 (1993)
32. Voskresensky V M et al. *Bull. Russ. Acad. Sci. Phys.* **82** 322 (2018); *Izv. Ross. Akad. Nauk. Ser. Fiz.* **82** (3) 369 (2018)
33. Sidorov N V et al. *J. Solid State Chem.* **282** 121109 (2020)
34. Aleshina L A et al. *Inorg. Mater.* **55** 692 (2019); *Neorgan. Mater.* **55** 738 (2019)
35. Kadetova A V et al. *Materialia* **28** 101770 (2023)
36. Kong Y et al. *J. Appl. Phys.* **87** 4410 (2000)
37. Palatnikov M N et al. *Defektnaya Struktura Kristallov Niobata Litiya Odinarnogo i Dvoinogo Legirivaniya* (Defect Structure of Single and Double Doped Lithium Niobate Crystals) (Moscow: RAN, 2024)
38. Kumada N et al. *J. Solid State Chem.* **57** 267 (1985)
39. Sun W-B et al. *J. Luminescence* **184** 191 (2017)
40. Kong T et al. *Materials* **12** (24) 4155 (2019)
41. Kong T et al. *Materials* **14** (4)1017 (2021)
42. Liu J et al. *Physica B* **624** 413419 (2022)
43. Palatnikov M N et al. *Opt. Mater.* **131** 112631 (2022)
44. Zhang P et al. *Opt. Mater.* **36** 1986 (2014)
45. Palatnikov M N et al. *Crystallogr. Rep.* **65** (1) 18 (2020); *Kristallografiya* **65** (1) 23 (2020)
46. Palatnikov M N et al. *J. Am. Ceram. Soc.* **100** 3703 (2017)
47. Sidorov N V et al. *Lazernaya Konoskopiya i Fotoindutsirovannoe Rasseyanie Sveta v Issledovaniyakh Svoistv Nelineino-Opticheskogo Kristalla Niobata Litiya* (Laser Conoscopy and Photoinduced Light Scattering in Property Investigations of Nonlinear-Optical Lithium Niobate Crystal) (Moscow: RAN, 2019)
48. Pikoul O *J. Appl. Cryst.* **43** 955 (2010)
49. Maksimenko V A, Syui A V, Karpets Yu M *Fotoindutsirovannye Protsessy v Kristallakh Niobata Litiya* (Photoinduced Processes in Lithium Niobate Crystals) (Moscow: Fizmatlit, 2008)
50. Syuy A V et al. *Optik* **156** 239 (2018)
51. Palatnikov M N et al. *Perspektivnye Mater.* (2) 93 (2011)
52. Palatnikov M N, Sidorov N V "Ch. 2. Some fundamental points of technology of lithium niobate and lithium tantalite single crystals," in *Oxide Electronics and Functional Properties of Transition Metal Oxides* (Ed. A Pergament) (Hauppauge, NY: NOVA Science Publ., 2014) p. 31
53. Palatnikov M N et al. *J. Cryst. Growth* **386** 113 (2014)
54. Anikiev A A et al. *Opt. Mater.* **111** 110729 (2021)
55. Anderson A (Ed.) *The Raman Effect* Vol. 2 *Applications* (New York: M. Dekker, 1973)
56. Gorelik V S, Sverbil' P P *Inorg. Mater.* **51** 1104 (2015); *Neorgan. Mater.* **51** 1190 (2015)
57. Gorelik V S, Abdurakhmonov S D *Crystallogr. Rep.* **67** 252 (2022); *Kristallografiya* **67** 295 (2022)
58. Abdurakhmonov S D, Gorelik V S *Opt. Spectrosc.* **127** 587 (2019); *Opt. Spektrosk.* **127** 532 (2019)
59. Sidorov N V et al. *Spectrochim. Acta A* **266** 120445 (2022)
60. Sidorov N V et al. *Opt. Mater.* **134** 113137 (2022)
61. Surovtsev N V et al. *Phys. Solid State* **45** 534 (2003); *Fiz. Tverd. Tela* **45** 505 (2003)
62. Anikiev A A, Umarov M F, Scott J F *AIP Adv.* **8** 115016 (2018)
63. Anikiev A A, Umarov M F *Opt. Spectrosc.* **125** 22 (2018); *Opt. Spektrosk.* **125** 19 (2018)
64. Nogueira B A et al. *J. Raman Spectrosc.* **52** 995 (2021)
65. Claus R et al. *Z. Naturforsch. A* **27** 1187 (1972)
66. Yang X et al. *Phys. Status Solidi B* **142** 287 (1987)
67. Gorelik V S *Trudy Fiz. Inst. Akad. Nauk* **132** 15 (1982)
68. Schuller E et al. *Z. Naturforsch. A* **32** (1) 47 (1977)
69. Sidorov N V et al. *Fononnye Spektry Monokristallov Niobata Litiya* (Phonon Spectra of Lithium Niobate Single Crystals) (Exec. Ed. V T Kalinnikov) (Apatity: KNTs RAN, 2012)
70. Donnerberg H J, Tomlinson S M, Catlow C R A *J. Phys. Chem. Solids* **52** 201 (1991)
71. Ridah A et al. *J. Phys. Condens. Matter* **9** 9687 (1997)

72. Anikiev A A *Inzh. Zh. Nauka Innovatsii* (7) (2013)
73. Sanna S et al. *Phys. Rev. B* **91** 224302 (2015)
74. Maïmounatou B, Mohamadou B, Erasmus R *Phys. Status Solidi B* **253** 573 (2016)
75. Parlinski K, Li Z Q, Kawazoe Y *Phys. Rev. B* **61** 272 (2000)
76. Repelin Y et al. *J. Phys. Chem. Solids* **60** 819 (1999)
77. Sidorov N et al. *Appl. Sci.* **13** 2348 (2023)
78. Palatnikov M et al. *Photonics* **10** 439 (2023)
79. Titov R et al. *Crystals* **13** 1245 (2023)
80. Friedrich M et al. *J. Phys. Condens. Matter* **27** 385402 (2015)
81. Aillerie M et al. *J. Phys. Conf. Ser.* **416** 012001 (2013)
82. Fedorova E P et al. *Inorg. Mater.* **46** 206 (2010); *Neorgan. Mater.* **46** (2) 247 (2010)
83. Bartasyte A et al. *J. Phys. Condens. Matter* **25** 205901 (2013)
84. Sidorov N V et al. *Inorg. Mater.* **33** 419 (1997); *Neorgan. Mater.* **33** 496 (1977)
85. Voron'ko Yu K et al. *Fiz. Tverd. Tela* **29** 1348 (1987)
86. Voron'ko Yu K et al. *Trudy Inst. Obshch. Fiz. Akad. Nauk* **29** 50 (1991)
87. Voskresenskii V M et al. *Crystallogr. Rep.* **62** 205 (2017); *Kristallografiya* **62** (2) 213 (2017)
88. Kumada N, Kinomura N, Muto F *J. Ceram. Soc. Jpn.* **98** 384 (1990)
89. Smyth D M *Ferroelectrics* **50** 93 (1983)
90. Maaider K, Masaif N, Khalil A *Indian J. Phys.* **95** 275 (2020)
91. Kumada N et al. *J. Solid State Chem.* **57** 267 (1985)
92. Ko J, Prewitt C T *Phys. Chem. Minerals* **15** 355 (1988)
93. Baran E J et al. *J. Mater. Sci. Lett.* **5** 671 (1986)
94. Sidorov N et al. *Photonics* **10** 921 (2023)
95. Palatnikov M N et al. *Opt. Mater.* **135** 113241 (2023)